

Reconstructions of time-evolving sound-speed fields perturbed by deformed and dispersive internal solitary waves in shallow water

Qin-Ran Li(李沁然), Chao Sun(孙超), Lei Xie(谢磊), and Xiao-Dong Huang(黄晓冬)
Citation: Chin. Phys. B, 2023, 32 (**12**): 124701. DOI: 10.1088/1674-1056/acf84d
Journal homepage: http://cpb.iphy.ac.cn; http://iopscience.iop.org/cpb

What follows is a list of articles you may be interested in

Simulation of gas-liquid two-phase flow in a flow-focusing microchannel with the lattice Boltzmann method

Kai Feng(冯凯), Gang Yang(杨刚), and Huichen Zhang(张会臣)
Chin. Phys. B, 2023, 32 (**11**): 114703. DOI: 10.1088/1674-1056/acea6e

Discussion on interface deformation and liquid breakup mechanism in vapor-liquid two-phase flow

Xiang An(安祥), Bo Dong(董波), Ya-Jin Zhang(张雅瑾), and Xun Zhou(周训)
Chin. Phys. B, 2023, 32 (**9**): 094702. DOI: 10.1088/1674-1056/acc78e

Improved contact angle measurement in multiphase lattice Boltzmann

Xing-Guo Zhong(钟兴国), Yang-Sha Liu(刘阳莎), Yi-Chen Yao(姚怡辰), Bing He(何冰), and Bing-Hai Wen(闻炳海)
Chin. Phys. B, 2023, 32 (**5**): 054701. DOI: 10.1088/1674-1056/ac9cbd

Simulation of single bubble dynamic process in pool boiling process under microgravity based on phase field method

Chang-Sheng Zhu(朱昶胜), Bo-Rui Zhao(赵博睿), Yao Lei(雷瑶), and Xiu-Ting Guo(郭秀婷)
Chin. Phys. B, 2023, 32 (**4**): 044702. DOI: 10.1088/1674-1056/aca209

Lattice Boltzmann model for interface capturing of multiphase flows based on Allen-Cahn equation

He Wang(王贺), Fang-Bao Tian(田方宝), and Xiang-Dong Liu(刘向东)
Chin. Phys. B, 2022, 31 (**2**): 024701. DOI: 10.1088/1674-1056/ac11d8

Reconstructions of time-evolving sound-speed fields perturbed by deformed and dispersive internal solitary waves in shallow water

Qin-Ran Li(李沁然)[1,2], Chao Sun(孙超)[1,2,3,†], Lei Xie(谢磊)[1,2,‡], and Xiao-Dong Huang(黄晓冬)[4,5,6]

[1] *School of Marine Science and Technology, Northwestern Polytechnical University, Xi'an* 710072, *China*
[2] *Shaanxi Key Laboratory of Underwater Information Technology, Xi'an* 710072, *China*
[3] *Qingdao Research Institute, Northwestern Polytechnical University, Qingdao* 266200, *China*
[4] *Frontier Science Center for Deep Ocean Multispheres and Earth System (FDOMES) and Physical Oceanography Laboratory, Ocean University of China, Qingdao* 266100, *China*
[5] *Key Laboratory of Ocean Observation and Information of Hainan Province and Sanya Oceanographic Institution, Ocean University of China, Sanya* 572024, *China*
[6] *Laoshan Laboratory, Qingdao* 266237, *China*

(Received 6 June 2023; revised manuscript received 20 August 2023; accepted manuscript online 11 September 2023)

The high-fidelity reconstruction of sound speeds is crucial for predicting acoustic propagation in shallow water where internal solitary waves (ISWs) are prevalent. Mapping temperatures from time series to spatial fields is an approach widely used to reproduce the sound speed perturbed by deformed internal waves. However, wave-shape distortions are inherent in the modeling results. This paper analyzes the formation mechanism and dynamic behavior of the distorted waveform that is shown to arise from the mismatch between the modeled and real propagation speeds of individual solitons within an ISW packet. To mitigate distortions, a reconstruction method incorporating the dispersion property of an ISW train is proposed here. The principle is to assign each soliton a real speed observed in the experiment. Then, the modeled solitons propagate at their intrinsic speeds, and the packet disperses naturally with time. The method is applied to reconstruct the sound speed perturbed by ISWs in the South China Sea. The mean and median of the root-mean-square error between the reconstructed and measured sound speeds are below 2 m/s. The modeled shape deformations and packet dispersion agree well with observations, and the waveform distortion is reduced compared with the original method. This work ensures the high fidelity of waveguide-environment reconstructions and facilitates the investigation of sound propagation in the future.

Keywords: internal solitary wave, deformation, dispersion, sound speed

PACS: 47.35.Fg, 46.40.Cd, 43.58.Dj **DOI:** 10.1088/1674-1056/acf84d

1. Introduction

Internal solitary waves (ISWs) with large amplitudes, high current velocities, and strong vertical shears are ubiquitous in the ocean.[1,2] ISWs may cause large fluctuations to sound-speed fields in the horizontal range and the vertical depth and further affect underwater acoustic propagation.[3] Previous work[4,5] suggests that the high-fidelity reconstructions of sound speeds in water are the essential prerequisites for studying sound transmission in the fluctuating medium. The frequently used approaches to synthesizing the space- and time-dependent sound speed can be divided into four categories: (1) theoretical methods based on the solutions to the Korteweg–de Vries (KdV) equation, such as the well-known hyperbolic secant profile and the dnoidal model,[6,7] (2) ocean numerical models, e.g., the MIT general circulation model (MITgcm)[8,9] and the MIT-multidisciplinary simulation, estimation, and assimilation systems (MIT-MSEAS),[10,11] (3) utilizations of data features, e.g., the empirical orthogonal function (EOF) representation[12] and the tensor dictionary learning,[13] and (4) hybrid techniques which, by coupling experimental data with physical models, maintain a better balance between the fidelity of modeling results and the convenience in model configurations for studying acoustic problems. Driven by both observed data and theoretical models, the hybrid-type reconstruction methods have received much attention,[14–16] and the single propagated thermistor string (SPTS) technique[17] is a representative. In SPTS, the temperature time series recorded by a thermistor string are advected at a constant speed along a track to simulate internal-wave propagation, and the modeled wave shapes do not change with time since they are solely derived from the observations of a single mooring. Afterwards, the evolutionary propagated thermistor string (EPTS) method[18–20] was developed to take into account the temporal evolution of internal-wave shapes by integrating the information from multiple-mooring data.

Both SPTS and EPTS have fully accounted for the shape deformations of internal waves, which include the variations of amplitude, the development or decay of solitons, and other changes in waveform structures. Nevertheless, severe shape distortions are found to be inherent in the sound speeds reproduced by EPTS that neglects the difference in propaga-

†Corresponding author. E-mail: csun@nwpu.edu.cn
‡Corresponding author. E-mail: xielei2014@mail.nwpu.edu.cn

© 2023 Chinese Physical Society and IOP Publishing Ltd

tion speeds among individual solitons within a wave train so that the modeled solitons propagate at the same speed as a whole. This paper demonstrates that the distorted waveform is caused by the mismatch between the modeled and real speeds of individual solitons in a packet and exhibits anomalous dynamic behavior during the modeled internal-wave propagation. To address this deficiency, our work here proposes a dispersive evolutionary propagated thermistor string (DEPTS) technique which, by assigning each soliton its real speed instead of the same one as others, models the ISW packet with the dispersion property incorporated. Besides, the DEPTS model weights the data collected by different moorings according to the distances from them to reproduce the time-varying wave shapes. Thus, shape deformations and packet dispersion, the two internal-wave properties significantly affecting acoustic propagation,[5,21,22] are both incorporated into the DEPTS model. In addition, while modeling the evolution process of internal waves, DEPTS also successfully eliminates the shape distortion in the original method, thus ensuring the physical significance of the dynamic behavior of reconstructed sound speeds.

The rest of this paper is organized as follows. In Section 2, after presenting some essential concepts of internal waves, the formation mechanism and dynamic behavior of the waveform distortion in EPTS are analyzed in a general waveguide model. In Section 3, the DEPTS method is developed, and the fidelity of the DEPTS-modeled wave shapes is examined. In Section 4, the configuration and observations in a sea trial conducted in the northern South China Sea (SCS) are reviewed. And then, in Section 5, the DEPTS method is applied to reconstruct the sound-speed fields during the evolution of internal waves. The temporal variations of sound speeds modeled by DEPTS are compared with *in-situ* observations quantitatively by calculating the root-mean-square error (RMSE). A comparison between the sound-speed fields reconstructed by DEPTS and EPTS is also made in the range-depth plane to examine the effectiveness of DEPTS in mitigating the waveform distortion. Finally, a summary of this paper and some important conclusions are given in Section 6.

2. Problem formulation of reconstructions

2.1. Basics of internal waves

Internal-wave amplitudes can be characterized by isothermal displacements $\eta(r,z,t)$, and the perturbed temperature field takes the form[18]

$$T(r,z,t) = \bar{T}(r, z-\eta(r,z,t), t), \tag{1}$$

where $\bar{T}(r,z,t)$ is the background temperature field in the absence of internal waves. A coordinate system (r,z,t) is adopted in this study with r, z, and t denoting the horizontal range, the vertical depth, and time, respectively, and the z-axis is positive in the downward direction.

According to the normal mode method,[3,23] $\eta(r,z,t)$ can be expressed as

$$\eta(r,z,t) = \sum_n A_n(r,t) W_n(z), \tag{2}$$

where $A_n(r,t)$ and $W_n(z)$ are the amplitude and modal function of mode n, respectively. The modal function $W_n(z)$ obeys the Taylor–Goldstein equation[3,24,25]

$$\frac{\mathrm{d}^2 W_n(z)}{\mathrm{d}z^2} + \frac{N^2(z)}{v_n^2} W_n(z) = 0 \tag{3}$$

and satisfies the rigid-lid boundary condition

$$W_n(z=0) = W_n(z=H) = 0, \tag{4}$$

where eigenvalue v_n is the linear wave speed of mode n, and H is the water depth. The buoyancy frequency $N(z)$ is given by

$$N(z) = \sqrt{\frac{g}{\bar{\rho}(z)} \frac{\mathrm{d}\bar{\rho}(z)}{\mathrm{d}z}}, \tag{5}$$

where $\bar{\rho}(z)$ is the background density profile, and g is the gravitational acceleration.

2.2. Waveguide model

In reality, generally only a limited number of moorings are sparsely deployed in the experimental area. Then, a challenging issue is how to reconstruct the space- and time-dependent internal-wave field $\eta(r,z,t)$ from the temperatures $T(z,t;r_{\mathrm{id}})$ measured by moorings, where id is the identifier of mooring id deployed at range $r = r_{\mathrm{id}}$. Next, a simple and general scenario for reconstructing sound-speed fields is described.

As shown in Fig. 1, the waveguide considered in this paper is two-dimensional in space with range r and depth z. Two oceanographic moorings are deployed along a track in the range from $r = r_i$ and r_j, with $r_i < r_j$. Temperature-pressure (TP) sensors are mounted on the moorings to record the temperatures in the water column. An ISW packet containing two individual solitary waves called solitons 1 and 2 propagates from mooring j to mooring i. Soliton 1 with a larger amplitude is nearer the front of the packet and propagates faster than soliton 2, as generally observed in experiments and anticipated by the theory. For simplicity, the wave polarity in all schematic diagrams in Sections 2 and 3 is designated as depression. It should be noted that the waveform polarity of an ISW depends on the stratification property of the water column in reality. The choice of polarity in schematics throughout this

paper is arbitrary, just for intuitively describing the reconstruction methods.

To facilitate the following derivation, we now suppose that wave-amplitude profiles $\eta(z,t;r_{\rm id})$ have been calculated from temperature measurements $T(z,t;r_{\rm id})$ and have been decomposed into normal modes to obtain modal amplitudes $A_n(t;r_{\rm id})$.

2.3. Shape distortions in the EPTS-modeled ISWs

2.3.1. Brief introduction to EPTS

Using the property of plane-wave propagation, EPTS maps temporal waveforms $A_n(t;r_i)$ and $A_n(t;r_j)$ to horizontally progressive wave fields as a function of range r and time t, written as

$$A_n(r,t;r_i)=A_n\left(t+\frac{r-r_i}{v^{(1)}_{{\rm P},i-j}};r_i\right), \tag{6a}$$

$$A_n(r,t;r_j)=A_n\left(t+\frac{r-r_j}{v^{(1)}_{{\rm P},i-j}};r_j\right), \tag{6b}$$

where

$$v^{(k)}_{{\rm P},i-j}=\frac{r_i-r_j}{t^{(k)}_{{\rm P},j}-t^{(k)}_{{\rm P},i}} \tag{7}$$

is the peak speed of soliton k on track i–j, and $t^{(k)}_{{\rm P,id}}$ is the peak arrival time of soliton k at mooring id. It can be seen that the propagation speed of the packet is designated as a single value $v^{(1)}_{{\rm P},i-j}$ in EPTS. Considering the moving direction ($j\to i$) of the packet shown in Fig. 1 gives $t^{(1)}_{{\rm P},i}>t^{(1)}_{{\rm P},j}$ and $t^{(2)}_{{\rm P},i}>t^{(2)}_{{\rm P},j}$.

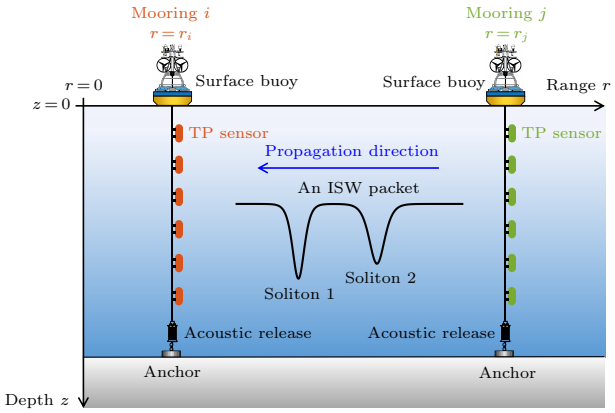


Fig. 1. Scenario for reconstructing sound-speed fields, including mooring configurations and the features of internal waves.

As an evolutionary model, EPTS requires the fusion of waveforms $A_n(r,t;r_i)$ and $A_n(r,t;r_j)$ from both moorings and reconstructs the fused wave shape

$$A_n(r,t)=w_i(r)A_n(r,t;r_i)+w_j(r)A_n(r,t;r_j), \tag{8}$$

where $w_i(r)$ and $w_j(r)$ are weighting functions and are not unique in EPTS.[18] They are generally determined according to the following two criteria: (1) the nearer to mooring id, the larger the $w_{\rm id}(r)$; (2) $w_i(r)+w_j(r)=1$. Equation (8) indicates that the range-dependent weighting functions control the similarity between the fused waveform $A_n(r,t)$ and its two components, i.e., $A_n(r,t;r_i)$ and $A_n(r,t;r_j)$. Thus, $A_n(r,t)$ keeps deforming when propagating along range r, and an important evolving property, i.e., shape deformation, is now reconstructed by EPTS.

2.3.2. Formation mechanism of distortions

Since the waveform fusion described by Eq. (8) involves the coherent superposition of two traveling waves, the phase consistency between the same solitons in $A_n(r,t;r_i)$ and $A_n(r,t;r_j)$ ensures that the reconstructed waveform $A_n(r,t)$ is undistorted. Next, taking a snapshot fixed at a given time instant as an example, the waveform fusion is analyzed in detail to investigate the manifestation and cause of shape distortions in EPTS. Examples of $A_n(r,t_0;r_i)$, $A_n(r,t_0;r_j)$, and $A_n(r,t_0)$ in a snapshot at time $t=t_0$ are shown in Fig. 2 by the red, green, and black lines, respectively. The difference in crest positions between solitons in $A_n(r,t_0;r_i)$ and $A_n(r,t_0;r_j)$ is chosen as the metric to quantify the phase consistency. Ideally, if the peak position of soliton k in $A_n(r,t_0;r_i)$ coincides with that in $A_n(r,t_0;r_j)$, the waveforms of soliton k in $A_n(r,t_0;r_i)$ and $A_n(r,t_0;r_j)$ are in phase. Conversely, both of them are out of phase.

The relationship between the crest positions of soliton 1 in $A_n(r,t_0;r_i)$ and $A_n(r,t_0;r_j)$ is determined as follows. Referring to the temporal-spatial mapping described by Eqs. (6a) and (6b), let $r=r^{(1)}_{{\rm P},i}$ be the wave crest position of soliton 1 in $A_n(r,t_0;r_i)$, which yields

$$A_n\left(r^{(1)}_{{\rm P},i},t_0;r_i\right)=A_n\left(t_0+\frac{r^{(1)}_{{\rm P},i}-r_i}{v^{(1)}_{{\rm P},i-j}};r_i\right)=A_n\left(t^{(1)}_{{\rm P},i};r_i\right). \tag{9}$$

Solving Eq. (9) gives an intermediate variable, i.e., time instant t_0, expressed as

$$t_0=t^{(1)}_{{\rm P},i}-\frac{r^{(1)}_{{\rm P},i}-r_i}{v^{(1)}_{{\rm P},i-j}}. \tag{10}$$

To find out the crest position of soliton 1 in $A_n(r,t;r_j)$, substituting Eq. (10) into Eq. (6b) results in

$$\begin{aligned}A_n(r,t_0;r_j)&=A_n\left(t_0+\frac{r-r_j}{v^{(1)}_{{\rm P},i-j}};r_j\right)\\&=A_n\left(t^{(1)}_{{\rm P},i}+\frac{r-r^{(1)}_{{\rm P},i}+r_i-r_j}{v^{(1)}_{{\rm P},i-j}};r_j\right).\end{aligned} \tag{11}$$

According to Eq. (7), the speed of soliton 1 is given by

$$v^{(1)}_{{\rm P},i-j}=\frac{r_i-r_j}{t^{(1)}_{{\rm P},j}-t^{(1)}_{{\rm P},i}}, \tag{12}$$

and then Eq. (11) is reduced to

$$A_n(r,t_0;r_j)=A_n\left(t_{\mathrm{P},j}^{(1)}+\frac{r-r_{\mathrm{P},i}^{(1)}}{v_{\mathrm{P},i-j}^{(1)}};r_j\right). \tag{13}$$

To localize the crest of soliton 1 in $A_n(r,t_0;r_j)$, let the phase in the last term of Eq. (13) be equal to $t_{\mathrm{P},j}^{(1)}$, i.e.,

$$t_{\mathrm{P},j}^{(1)}+\frac{r-r_{\mathrm{P},i}^{(1)}}{v_{\mathrm{P},i-j}^{(1)}}=t_{\mathrm{P},j}^{(1)}, \tag{14}$$

which reveals that the crest is also at $r=r_{\mathrm{P},i}^{(1)}$ and coincides with the first peak in $A_n(r,t_0;r_i)$, as shown by the blue arrow in Fig. 2.

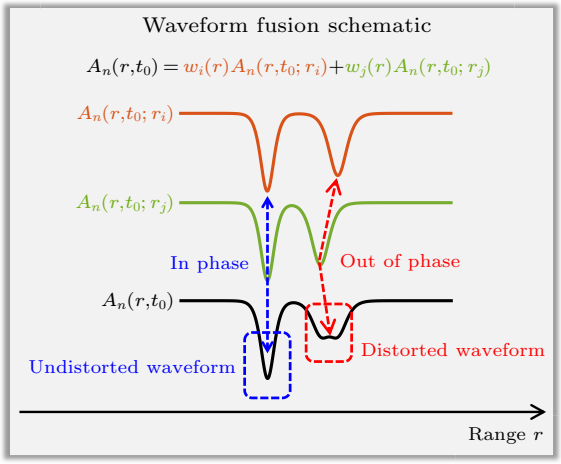


Fig. 2. Waveform fusion schematic of $A_n(r,t_0;r_i)$ (the red line), $A_n(r,t_0;r_j)$ (the green line), and $A_n(r,t_0)$ (the black line).

The above derivation also applies to soliton 2. Let $r=r_{\mathrm{P},i}^{(2)}$ be the crest position of soliton 2 in $A_n(r,t_0;r_i)$, which yields

$$A_n\left(r_{\mathrm{P},i}^{(2)},t_0;r_i\right)=A_n\left(t_0+\frac{r_{\mathrm{P},i}^{(2)}-r_i}{v_{\mathrm{P},i-j}^{(1)}};r_i\right)=A_n\left(t_{\mathrm{P},i}^{(2)};r_i\right), \tag{15}$$

and t_0 is given by

$$t_0=t_{\mathrm{P},i}^{(2)}-\frac{r_{\mathrm{P},i}^{(2)}-r_i}{v_{\mathrm{P},i-j}^{(1)}}. \tag{16}$$

Then, the crest of soliton 2 in $A_n(r,t_0;r_j)$ is localized by substituting Eq. (16) into Eq. (6b), i.e.,

$$\begin{aligned}A_n(r,t_0;r_j)&=A_n\left(t_0+\frac{r-r_j}{v_{\mathrm{P},i-j}^{(1)}};r_j\right)\\&=A_n\left(t_{\mathrm{P},i}^{(2)}+\frac{r-r_{\mathrm{P},i}^{(2)}+r_i-r_j}{v_{\mathrm{P},i-j}^{(1)}};r_j\right),\end{aligned} \tag{17}$$

and by letting the phase in the last term of Eq. (17) be equal to $t_{\mathrm{P},j}^{(2)}$, i.e.,

$$t_{\mathrm{P},i}^{(2)}+\frac{r-r_{\mathrm{P},i}^{(2)}+r_i-r_j}{v_{\mathrm{P},i-j}^{(1)}}=t_{\mathrm{P},j}^{(2)}. \tag{18}$$

Solving Eq. (18) shows that the crest of soliton 2 in $A_n(r,t_0;r_j)$ is in the range of

$$r=r_{\mathrm{P},j}^{(2)}=r_{\mathrm{P},i}^{(2)}+\frac{v_{\mathrm{P},i-j}^{(1)}-v_{\mathrm{P},i-j}^{(2)}}{v_{\mathrm{P},i-j}^{(2)}}(r_i-r_j), \tag{19}$$

where $v_{\mathrm{P},i-j}^{(2)}=(r_i-r_j)/(t_{\mathrm{P},j}^{(2)}-t_{\mathrm{P},i}^{(2)})$ is the practical propagation speed of soliton 2 on the track. Due to $v_{\mathrm{P},i-j}^{(1)}>v_{\mathrm{P},i-j}^{(2)}$, Eq. (19) reveals that the crest positions of soliton 2 in $A_n(r,t_0;r_i)$ and $A_n(r,t_0;r_j)$ do not coincide at r, which is indicated by the red arrow in Fig. 2.

As formulated in Eqs. (6a) and (6b), since EPTS uses the same propagation speed for both solitons that travel at different speeds in reality, the waveform distortion (see the red box in Fig. 2) is unavoidable in EPTS.

2.3.3. Dynamic behavior of waveform distortions

In this section, by taking multiple snapshots at different time instants as examples, the dynamic behavior of the distorted waveform during internal-wave propagation is further studied. Figures 3(a), 3(b), and 3(c) extend the single snapshot in Fig. 2 to three snapshots at time instants $t=t_0^-$, t_0, and t_0^+ when the packet is near mooring j, in the middle, and is near mooring i, respectively. The comparison of Figs. 3(a)–3(c) reveals that the waveforms of soliton 1 in $A_n(r,t;r_i)$ and $A_n(r,t;r_j)$ are consistently in phase, whereas the two wave crests of soliton 2 do not coincide at r with a constant range difference due to the speed mismatch, as indicated by Eq. (19).

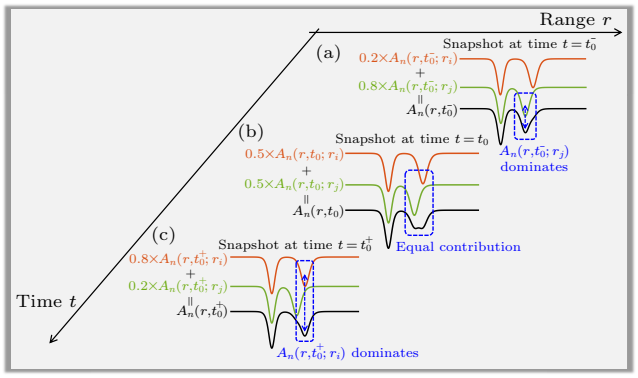


Fig. 3. Schematics of the dynamic shape behavior of internal waves modeled by the EPTS method at times (a) $t=t_0^-$, (b) $t=t_0$, and (c) $t=t_0^+$ when the wave train is near mooring j, in the midpoint of track i–j, and is near mooring i, respectively.

In addition, the shapes of $A_n(r,t)$ are highly variable among different snapshots. Figure 3(a) shows that $A_n(r,t_0^-;r_j)$ with a weighting of 80% dominates the shape of $A_n(r,t_0^-)$, and that the shape of soliton 2 in $A_n(r,t_0^-)$ bears more resemblance to that in $A_n(r,t_0^-;r_j)$. The wave crests of soliton 2 in $A_n(r,t_0^-)$ and $A_n(r,t_0^-;r_j)$ are almost at the same position, as indicated by the blue-dashed box. Figure 3(b) is the case when $A_n(r,t_0;r_i)$ and $A_n(r,t_0;r_j)$ contribute equally to $A_n(r,t_0)$. The

non-constructive superposition of $A_n(r,t_0;r_i)$ and $A_n(r,t_0;r_j)$ gives rise to a severely distorted waveform of soliton 2 in $A_n(r,t_0)$ without an identifiable wave peak. On the contrary to Fig. 3(a), Fig. 3(c) shows the case when $A_n(r,t_0^+;r_i)$ accounts for 80% of the total weighting and thus dominates the shape of $A_n(r,t_0^+)$. The crest position of soliton 2 in $A_n(r,t_0^+)$ almost coincides with that in $A_n(r,t_0^+;r_i)$.

Comparing only Figs. 3(a) and 3(c), it is clear that the spacing between the two solitons does change with time, which looks the same as packet dispersion. However, continuing with Fig. 3(b) and the above analysis, it is demonstrated that the speed mismatch and the range dependency of weighting functions together give rise to the distortion of soliton 2 in the EPTS-modeled evolution process. This anomalous waveform behavior resulted from the deficiencies of EPTS cannot reflect the true dispersion property.

3. Dispersive evolutionary propagated thermistor string (DEPTS) model

3.1. Development of the DEPTS model

In this section, the DEPTS model is proposed to mitigate the distortions in the EPTS-modeled wave shapes by assigning real propagation speeds to individual solitons in a wave train. The DEPTS model is implemented in the following 4 steps: (1) feature extraction of individual solitons, (2) temporal-spatial mapping, (3) waveform fusion, and (4) concatenation of all solitons. The details of DEPTS will be explained in the following sections based on the same scenario in Fig. 1.

3.1.1. Step 1: Feature extraction of individual solitons

The waveform $A_n^{(k)}(t;r_{\rm id})$ of soliton k is extracted from the entire wave packet arrival $A_n(t;r_{\rm id})$ by identifying the time instants when its peak and the leading and trailing edges arrive at mooring id, denoted by $t_{\rm P,id}^{(k)}$, $t_{\rm L,id}^{(k)}$, and $t_{\rm T,id}^{(k)}$, respectively. Here, the leading edge is defined as the front boundary of a soliton at r, and the trailing edge is the back boundary.

The identification results of $A_n(t;r_i)$ and $A_n(t;r_j)$ are shown in Figs. 4(a) and 4(b), respectively. Given that the ISW train propagates from mooring j to mooring i, one has $t_{{\rm L},i}^{(k)} > t_{{\rm L},j}^{(k)}$, $t_{{\rm P},i}^{(k)} > t_{{\rm P},j}^{(k)}$, and $t_{{\rm T},i}^{(k)} > t_{{\rm T},j}^{(k)}$. Moreover, the trailing edge of a soliton coincides with the leading edge of the following one in time, which implies

$$\begin{cases} t_{{\rm T},i}^{(1)} = t_{{\rm L},i}^{(2)}, \\ t_{{\rm T},j}^{(1)} = t_{{\rm L},j}^{(2)}; \end{cases} \tag{20}$$

$$\begin{cases} A_n^{(1)}(t_{{\rm T},i}^{(1)};r_i) = A_n^{(2)}(t_{{\rm L},i}^{(2)};r_i), \\ A_n^{(1)}(t_{{\rm T},i}^{(1)};r_j) = A_n^{(2)}(t_{{\rm L},i}^{(2)};r_j); \end{cases} \tag{21}$$

as shown in Fig. 4.

For soliton k, the mean propagation speeds of the wave crest and the leading and trailing edges between moorings i and j can be calculated from the temporal arrivals in Fig. 4 as

$$v_{{\rm L},i-j}^{(k)} = \frac{r_i - r_j}{t_{{\rm L},j}^{(k)} - t_{{\rm L},i}^{(k)}}, \tag{22a}$$

$$v_{{\rm P},i-j}^{(k)} = \frac{r_i - r_j}{t_{{\rm P},j}^{(k)} - t_{{\rm P},i}^{(k)}}, \tag{22b}$$

$$v_{{\rm T},i-j}^{(k)} = \frac{r_i - r_j}{t_{{\rm T},j}^{(k)} - t_{{\rm T},i}^{(k)}}, \tag{22c}$$

respectively.

From the fact that soliton 1 propagates faster than soliton 2, one finds

$$v_{{\rm P},i-j}^{(1)} > v_{{\rm P},i-j}^{(2)}. \tag{23}$$

Combining Eqs. (22b) with (23) yields

$$t_{{\rm P},i}^{(2)} - t_{{\rm P},i}^{(1)} > t_{{\rm P},j}^{(2)} - t_{{\rm P},j}^{(1)}, \tag{24}$$

which indicates that packet dispersion is manifested as the temporal spread in the observed arrival structures of internal waves.

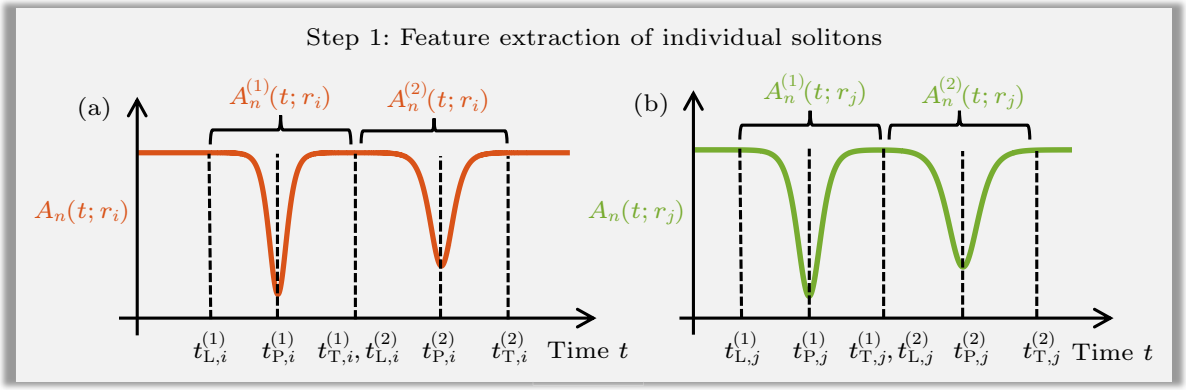


Fig. 4. Soliton identification results of (a) $A_n(t;r_i)$ and (b) $A_n(t;r_j)$. Here $t_{\rm P,id}^{(k)}$, $t_{\rm L,id}^{(k)}$, and $t_{\rm T,id}^{(k)}$ are the times when the crest and the leading and trailing edges of soliton k arrive at mooring id, respectively.

3.1.2. Step 2: Temporal-spatial mapping

First, the horizontal range where internal waves occur should be determined. With the speeds of two edges given by Eqs. (22a) and (22c), the front and back boundaries of soliton k are at

$$r_{\mathrm{L}}^{(k)}(t) = -v_{\mathrm{L},i-j}^{(k)}\left(t - t_{\mathrm{L},i}^{(k)}\right) + r_i, \tag{25a}$$

$$r_{\mathrm{T}}^{(k)}(t) = -v_{\mathrm{T},i-j}^{(k)}\left(t - t_{\mathrm{T},i}^{(k)}\right) + r_i, \tag{25b}$$

respectively. Soliton k is confined to the region $r_{\mathrm{L}}^{(k)}(t) \le r \le r_{\mathrm{T}}^{(k)}(t)$ when propagating along the track. Similar to Eqs. (25a) and (25b), the wave peak is at

$$r_{\mathrm{P}}^{(k)}(t) = -v_{\mathrm{P},i-j}^{(k)}(t - t_{\mathrm{P},i}^{(k)}) + r_i. \tag{26}$$

Then, the propagation speed of soliton k, assumed to change linearly with range, is given by

$$v_{i-j}^{(k)}(r;t) = \begin{cases} \dfrac{v_{\mathrm{L},i-j}^{(k)} - v_{\mathrm{P},i-j}^{(k)}}{r_{\mathrm{L}}^{(k)}(t) - r_{\mathrm{P}}^{(k)}(t)}\left(r - r_{\mathrm{P}}^{(k)}(t)\right) + v_{\mathrm{P},i-j}^{(k)}, & r_{\mathrm{L}}^{(k)}(t) \le r \le r_{\mathrm{P}}^{(k)}(t), \\ \dfrac{v_{\mathrm{T},i-j}^{(k)} - v_{\mathrm{P},i-j}^{(k)}}{r_{\mathrm{T}}^{(k)}(t) - r_{\mathrm{P}}^{(k)}(t)}\left(r - r_{\mathrm{P}}^{(k)}(t)\right) + v_{\mathrm{P},i-j}^{(k)}, & r_{\mathrm{P}}^{(k)}(t) < r \le r_{\mathrm{T}}^{(k)}(t). \end{cases} \tag{27}$$

Next, DEPTS individually maps the temporal arrival of soliton k to the range- and time-dependent waveform with its intrinsic speed $v_{i-j}^{(k)}(r;t)$. The traveling waveforms of soliton k derived from temporal modal amplitudes $A_n^{(k)}(t;r_i)$ and $A_n^{(k)}(t;r_j)$ are, respectively, written as

$$A_n^{(k)}(r,t;r_i) = A_n^{(k)}\left(t + \frac{r - r_i}{v_{i-j}^{(k)}(r;t)};r_i\right), \tag{28a}$$

$$A_n^{(k)}(r,t;r_j) = A_n^{(k)}\left(t + \frac{r - r_j}{v_{i-j}^{(k)}(r;t)};r_j\right). \tag{28b}$$

Comparing Eqs. (6a), (6b) and (28a), (28b), it can be seen that the mapping approach in DEPTS assigns each soliton k its own speed $v_{i-j}^{(k)}(r;t)$ instead of a common one $v_{\mathrm{P},i-j}^{(1)}$.

3.1.3. Step 3: Waveform fusion

Similar to EPTS, the waveform $A_n^{(k)}(r,t)$ of soliton k in DEPTS is expressed as the weighted average of $A_n^{(k)}(r,t;r_i)$ and $A_n^{(k)}(r,t;r_j)$, i.e.,

$$A_n^{(k)}(r,t) = w_i(r)A_n^{(k)}(r,t;r_i) + w_j(r)A_n^{(k)}(r,t;r_j), \tag{29}$$

which retains the features in both $A_n^{(k)}(r,t;r_i)$ and $A_n^{(k)}(r,t;r_j)$ at any time during propagation.

The linear weighting approach[26] is used in the implementation of the DEPTS model, and the range-dependent weighting functions are given by

$$\begin{cases} w_i(r) = -\frac{r - r_j}{r_j - r_i}, \\ w_j(r) = \frac{r - r_i}{r_j - r_i}. \end{cases} \tag{30}$$

Equations (29) and (30) indicate that, for the fused waveform $A_n^{(k)}(r,t)$, the contribution from $A_n^{(k)}(r,t;r_{\mathrm{id}})$ and thus the similarity to that increase (or decrease) as range r approaches (or moves away from) the mooring position $r = r_{\mathrm{id}}$.

3.1.4. Step 4: Concatenation of all solitons

Up to this point, individual waveforms $A_n^{(1)}(r,t)$ and $A_n^{(2)}(r,t)$ have been reproduced for solitons 1 and 2, respectively. To ensure that $A_n^{(1)}(r,t)$ and $A_n^{(2)}(r,t)$ can be recombined to construct a complete ISW packet, two kinds of continuity conditions need to be satisfied. First, the two intervals where the two solitons are present, i.e., $r_{\mathrm{L}}^{(1)}(t) \le r \le r_{\mathrm{T}}^{(1)}(t)$ and $r_{\mathrm{L}}^{(2)}(t) \le r \le r_{\mathrm{T}}^{(2)}(t)$, need to be continuous. Second, the waveforms $A_n^{(1)}(r,t)$ and $A_n^{(2)}(r,t)$ at the interface of the above two intervals, i.e., $A_n^{(1)}(r_{\mathrm{T}}^{(1)}(t),t)$ and $A_n^{(2)}(r_{\mathrm{L}}^{(2)}(t),t)$, need to be continuous. These two conditions, termed the interval continuity condition and the waveform continuity condition, respectively, will be demonstrated in the following.

According to the statement that the trailing edge of a soliton arrives at the same time as the leading edge of the following one at a mooring (cf. Eq. (20)), combining Eqs. (22a) and (22c) shows that the trailing edge of soliton 1 and the leading edge of soliton 2 propagate at the same speed, i.e.,

$$v_{\mathrm{T},i-j}^{(1)} = v_{\mathrm{L},i-j}^{(2)}. \tag{31}$$

Substituting Eqs. (20) and (31) into Eqs. (25a) and (25b) yields

$$r_{\mathrm{T}}^{(1)}(t) = r_{\mathrm{L}}^{(2)}(t), \tag{32}$$

indicating that the interval continuity condition is satisfied.

Then, substituting Eq. (27) into Eqs. (28a) and (28b) and referring to Eqs. (21), (25a), and (25b) produce

$$\begin{cases} A_n^{(1)}(r_{\mathrm{T}}^{(1)}(t),t;r_i) = A_n^{(2)}(r_{\mathrm{L}}^{(2)}(t),t;r_i), \\ A_n^{(1)}(r_{\mathrm{T}}^{(1)}(t),t;r_j) = A_n^{(2)}(r_{\mathrm{L}}^{(2)}(t),t;r_j). \end{cases} \tag{33}$$

Combining Eqs. (29), (32), and (33) leads to the continuity of waveforms between the two adjacent solitons:

$$A_n^{(1)}(r_{\mathrm{T}}^{(1)}(t),t) = A_n^{(2)}\left(r_{\mathrm{L}}^{(2)}(t),t\right). \tag{34}$$

Now, $A_n^{(1)}(r,t)$ and $A_n^{(2)}(r,t)$ can be directly concatenated along range r to construct a complete wave train

$$A_n(r,t)=\begin{cases}A_n^{(1)}(r,t), & r_{\rm L}^{(1)}(t)\le r\le r_{\rm T}^{(1)}(t),\\ A_n^{(2)}(r,t), & r_{\rm L}^{(2)}(t)< r\le r_{\rm T}^{(2)}(t).\end{cases} \tag{35}$$

3.2. Examination of the DEPTS-modeled waveform

In this section, the phase consistency between $A_n^{(k)}(r,t)$ and $A_n^{(k)}(r,t;r_{\rm id})$ is examined by a method similar to the one used in Subsection 2.3.2. Referring to Eqs. (27) and (28a), let $r=r_{{\rm P},i}^{(k)}$ be the peak position of $A_n^{(k)}(r,t_0;r_i)$ at a given time instant $t=t_0$, which yields

$$\begin{aligned}A_n^{(k)}\left(r_{{\rm P},i}^{(k)},t_0;r_i\right)&=A_n^{(k)}\left(t_0+\frac{r_{{\rm P},i}^{(k)}-r_i}{v_{{\rm P},i-j}^{(k)}};r_i\right)\\&=A_n^{(k)}\left(t_{{\rm P},i}^{(k)};r_i\right).\end{aligned} \tag{36}$$

Then, t_0 is expressed as

$$t_0=t_{{\rm P},i}^{(k)}-\frac{r_{{\rm P},i}^{(k)}-r_i}{v_{{\rm P},i-j}^{(k)}}. \tag{37}$$

Substituting Eq. (37) into Eq. (28b) leads to

$$\begin{aligned}A_n^{(k)}\left(r,t_0;r_j\right)&=A_n^{(k)}\left(t_0+\frac{r-r_j}{v_{i-j}^{(k)}(r;t_0)};r_j\right)\\&=A_n^{(k)}\left(t_{{\rm P},i}^{(k)}-\frac{r_{{\rm P},i}^{(k)}-r_i}{v_{{\rm P},i-j}^{(k)}}+\frac{r-r_j}{v_{i-j}^{(k)}(r;t_0)};r_j\right).\end{aligned} \tag{38}$$

Let $r=r_{{\rm P},j}^{(k)}$ be the peak position of $A_n^{(k)}(r,t_0;r_j)$, which results in

$$A_n^{(k)}\left(t_{{\rm P},i}^{(k)}+\frac{r_{{\rm P},j}^{(k)}-r_{{\rm P},i}^{(k)}+r_i-r_j}{v_{{\rm P},i-j}^{(k)}};r_j\right)=A_n^{(k)}\left(t_{{\rm P},j}^{(k)};r_j\right). \tag{39}$$

Recalling the crest speed of soliton k given in Eq. (22b), solving Eq. (39) produces $r_{{\rm P},j}^{(k)}=r_{{\rm P},i}^{(k)}$, suggesting that the crest of $A_n^{(k)}(r,t_0;r_j)$ coincides with that of $A_n^{(k)}(r,t_0;r_i)$.

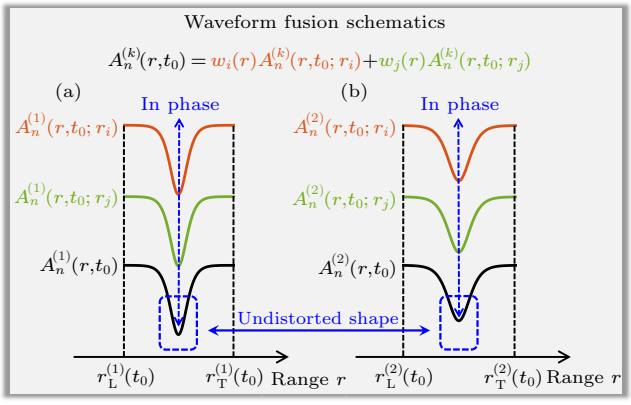


Fig. 5. Waveform fusion schematics of (a) soliton 1 and (b) soliton 2 at time $t=t_0$. $A_n^{(k)}(r,t_0;r_i)$, $A_n^{(k)}(r,t_0;r_j)$, and $A_n^{(k)}(r,t_0)$ are denoted by the red, green, and black lines, respectively.

The above derivation demonstrates that $A_n^{(k)}(r,t;r_i)$ and $A_n^{(k)}(r,t;r_j)$ are consistently in phase. For reference, the waveform fusion processes for solitons 1 and 2 at time instant $t=t_0$ are illustrated in Figs. 5(a) and 5(b), respectively. In contrast to the distorted waveform of soliton 2 in Fig. 2, the constructive superposition of $A_n^{(2)}(r,t_0;r_i)$ and $A_n^{(2)}(r,t_0;r_j)$ results in an undistorted solitary wave $A_n^{(2)}(r,t_0)$ as indicated by the blue box in Fig. 5(b).

4. Experiment overview and observations

4.1. Experiment description

A joint oceanographic-acoustic experiment was carried out in the northern SCS in July 2019. A total of four moorings were deployed along the ISW propagation path during the experiment, two of them were oceanographic moorings with TP sensors only, named IW1 and IW2, respectively. One was an acoustic mooring with a projector transmitting acoustic signals, referred to as TX. The last one was a hybrid mooring equipped both TP sensors and acoustic receivers (hydrophones), referred to as IW3. The mooring positions and the topography along the track are shown in Fig. 6, and the bathymetry data used in this paper are from the GEBCO database.[27] The water depth changed from 365 m (at IW1) to 327 m (at IW3) with a mild slope of 0.1°. Internal waves propagated from IW3 to IW1.

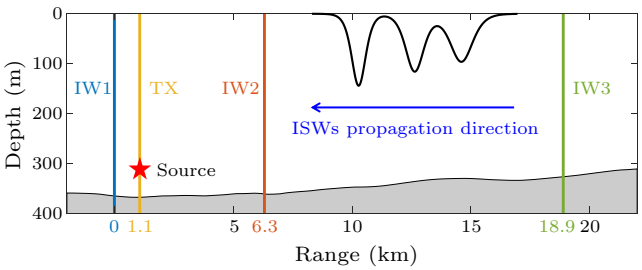


Fig. 6. Mooring positions and bathymetry on the track. Acoustic signals were transmitted by the source at TX and received by hydrophones at IW3. Internal waves propagated from IW3 to IW1.

IW1 and IW2 were deployed 6.3 km apart and were equipped with 24 and 26 TP sensors spanning the depths of 35–335 m and 35–325 m, respectively. The acoustic mooring TX was 1.1 km away from IW1 and contained a projector at 330.5-m depth. The hybrid mooring IW3 positioned 18.9 km away from IW1 was comprised of 20 hydrophones and 20 TP sensors spanning the depths of 55–245 m.

4.2. Case study of internal-wave evolution

A total of 25 internal wave events were observed during the experiment, and the 4th event (hereafter called Event 4) is chosen as the case to be analyzed and reconstructed in this paper due to its typical evolution process.

The evolution of Event 4 on track IW1–IW3 over the period of 07–10 18:23 to 07–11 02:04 (UTC+8) is shown

in Fig. 7. For convenience, the positions of moorings IW1, IW2, and IW3 are designated as $r_{\mathrm{IW1}} = 0$, $r_{\mathrm{IW2}} = 6.3$ km, and $r_{\mathrm{IW3}} = 18.9$ km, respectively. Temperatures at IW1, IW2, and IW3 are, respectively, shown in Figs. 7(a), 7(b), and 7(c) with the 22.5°C isotherms denoted by the blue lines and are used to calculate the sound speeds depicted in Figs. 7(d)–7(f). The arrows at the bottom of this figure denote the direction of internal-wave propagation.

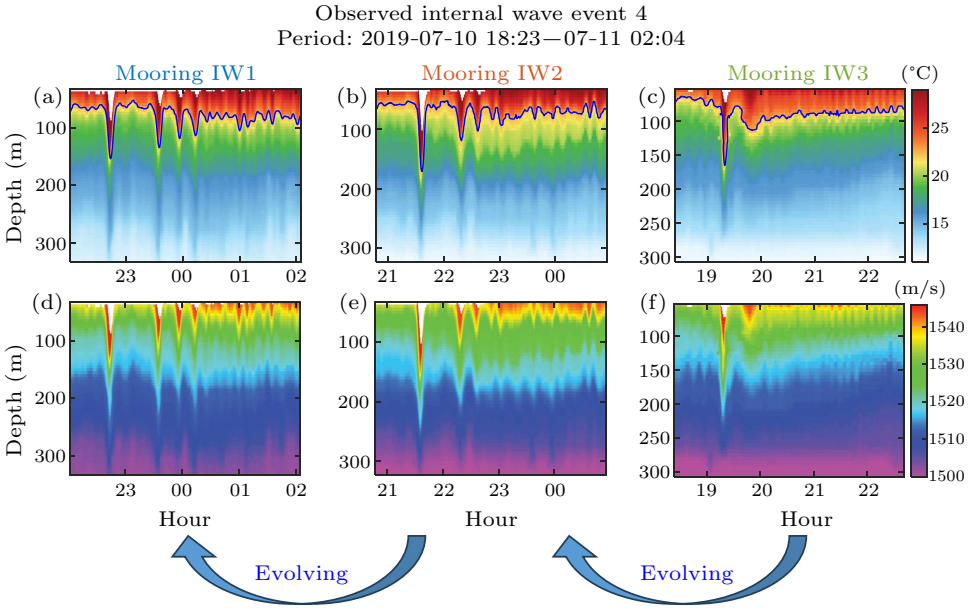


Fig. 7. Evolution process of Event 4 from 07–10 18:23 to 07–11 02:04 (UTC+8). (a)–(c) Temperatures with 22.5°C isotherms denoted by blue lines. (d)–(f) Sound-speed profiles. The arrows at the bottom indicate the propagation direction of internal waves.

It can be seen that the temporal variations of temperatures induced by ISWs create significant fluctuations in sound speeds. Both shape deformations and packet dispersion can be captured in Fig. 7. Specifically, the deformations include (i) the varying internal-wave amplitudes among the three moorings evidenced by the isothermal displacements in Figs. 7(a)–7(c) and (ii) the development of additional solitons in the ISW packet, as seen from the varying number of peaks in the 22.5°C isotherms. The dispersion is manifested as the spread of the temporal waveforms and is reflected in the longer delay between the peak arrivals of the first two solitons as indicated by the comparison of Figs. 7(a) and 7(c), which is in agreement with the description in Subsection 3.1.1.

Next, the DEPTS model will be used to reproduce the dynamic sound-speed fields during the evolution of Event 4.

5. Reconstruction of sound-speed fields perturbed by ISWs in the SCS

5.1. Implementation of DEPTS in the practical reconstruction

First, internal-wave amplitudes $\eta(z,t;r_{\mathrm{id}})$ are estimated from temperature measurements $T(z,t;r_{\mathrm{id}})$ at moorings id = IW1, IW2, and IW3 by the inverse mapping method.[4,28] Referring to Eq. (1), isothermal displacements are given by

$$\eta(z,t;r_{\mathrm{id}}) = z - \bar{T}^{-1}(T(z,t;r_{\mathrm{id}}),t;r_{\mathrm{id}}), \tag{40}$$

where $\bar{T}^{-1}(T,t;r_{\mathrm{id}})$ is the inverse function of the background temperatures $\bar{T}(z,t;r_{\mathrm{id}})$ that are obtained by applying a 48-h moving average filter to the *in-situ* data $T(z,t;r_{\mathrm{id}})$.

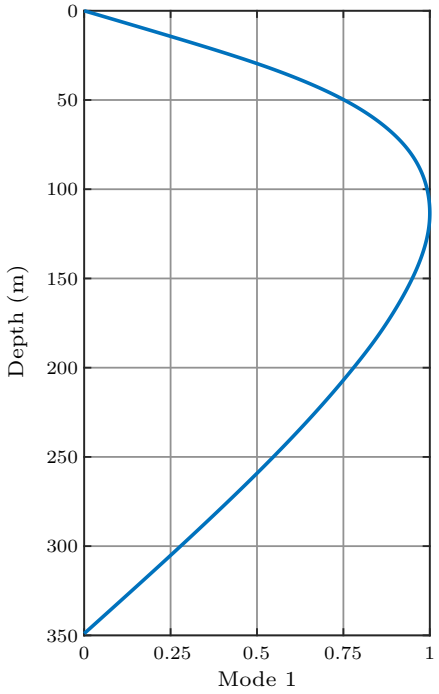


Fig. 8. The first-order modal function $W_1(z)$.

Then, the Sturm–Liouville problem expressed by Eqs. (3) and (4) is solved by the Thomson–Haskell method,[29] with a mean water depth of $H = 349$ m adopted in the boundary

condition. Given that the mode-1 depression waves dominated the observations in Event 4 and are more commonplace than mode-2 waves in the northern SCS,[30,31] only the mode-1 ISW train is modeled in this study. The modal function $W_1(z)$ is shown in Fig. 8.

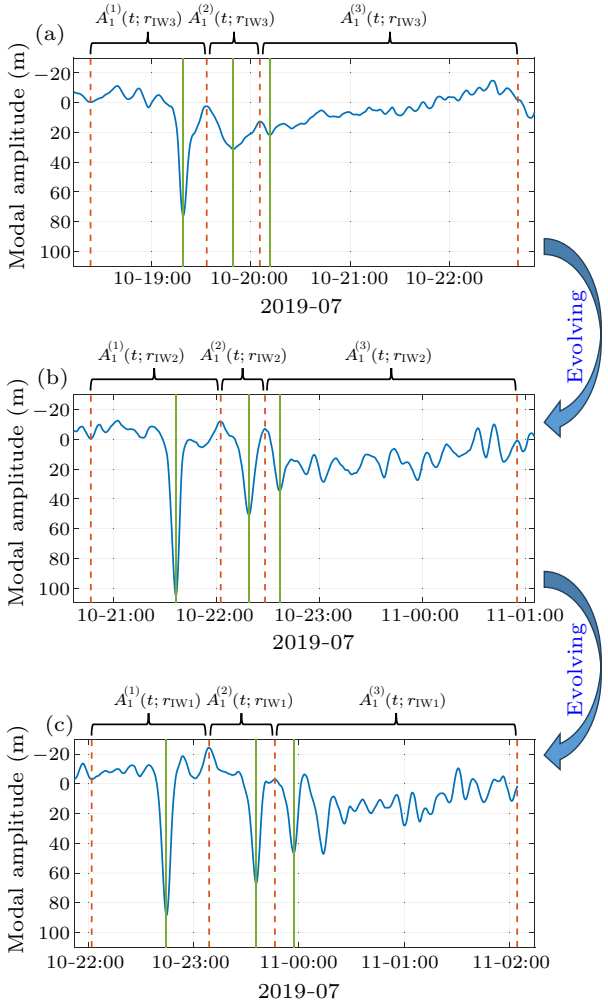


Fig. 9. Temporal waveforms (a) $A(t;r_{\rm IW3})$, (b) $A(t;r_{\rm IW2})$, and (c) $A(t;r_{\rm IW1})$. The red-dashed lines denote the times when the leading and trailing edges of solitons arrive at moorings, and the green-solid lines denote the arrival times of wave crests. The ISW propagation direction is indicated by two blue arrows.

Modal amplitudes $A_1(t;r_{\rm id})$ are estimated from isothermal displacements $\eta(z,t;r_{\rm id})$ by the least square method[32] and are given by

$$A_1(t;r_{\rm id}) = (W_1^{\rm T}(z)W_1(z))^{-1}W_1^{\rm T}(z)\eta(z,t;r_{\rm id}), \tag{41}$$

where the superscript T denotes the transpose operation. $A_1(t;r_{\rm id})$ at moorings id = IW3, IW2, and IW1 are shown in Figs. 9(a), 9(b), and 9(c), respectively. A total of three individual solitons are identified from the time series at each mooring, and thus $A_1(t;r_{\rm id})$ is divided into the following three segments:

$$A_1(t;r_{\rm id}) = \begin{cases} A_1^{(1)}(t;r_{\rm id}), & t_{\rm L,id}^{(1)} \le t < t_{\rm T,id}^{(1)}, \\ A_1^{(2)}(t;r_{\rm id}), & t_{\rm L,id}^{(2)} \le t < t_{\rm T,id}^{(2)}, \\ A_1^{(3)}(t;r_{\rm id}), & t_{\rm L,id}^{(3)} \le t \le t_{\rm T,id}^{(3)}, \end{cases} \tag{42}$$

as annotated at the top of each subplot in Fig. 9, where the red-dashed lines denote the leading and trailing edges of solitons, and the green-solid lines denote the wave crests. In addition, the two blue arrows indicate the propagation direction of internal waves (i.e., from IW3 to IW2 and then to IW1). The arrival times of the crest and the leading and trailing edges of soliton k at each mooring are given in Table 1. The propagation speeds of soliton k are subsequently obtained according to Eqs. (22a)–(22c) and are listed in Table 2.

Next, the waveforms $A_1^{(1)}(r,t)$, $A_1^{(2)}(r,t)$, and $A_1^{(3)}(r,t)$ of the three individual solitons are obtained by performing steps 2 and 3 described in Subsection 3.1 separately on tracks IW1–IW2 and IW2–IW3, and are concatenated to give a complete wave-packet shape $A_1(r,t)$. Referring to Eq. (2), the modeled internal-wave field can be written as

$$\eta(r,z,t) = A_1(r,t)W_1(z). \tag{43}$$

The background temperature $\bar{T}(r,z,t)$ is perturbed by internal waves $\eta(r,z,t)$, yielding the fluctuating temperature field

$$T(r,z,t) = \bar{T}(r,z-\eta(r,z,t),t), \tag{44}$$

where $\bar{T}(r,z,t)$ is obtained by interpolating $\bar{T}(z,t;r_{\rm id})$ (id = IW1,IW2,IW3) linearly along range r. Finally, the evolving sound-speed fields $c(r,z,t)$ are reconstructed from $T(r,z,t)$.

Table 1. Arrival times of the crest and the leading and trailing edges of soliton k at moorings IW1, IW2, and IW3.

	$t_{\rm L,IW3}^{(k)} - t_{\rm P,IW3}^{(k)} - t_{\rm T,IW3}^{(k)}$	$t_{\rm L,IW2}^{(k)} - t_{\rm P,IW2}^{(k)} - t_{\rm T,IW2}^{(k)}$	$t_{\rm L,IW1}^{(k)} - t_{\rm P,IW1}^{(k)} - t_{\rm T,IW1}^{(k)}$
$k=1$	18:23 – 19:19 – 19:33	20:47 – 21:36 – 22:02	22:02 – 22:44 – 23:09
$k=2$	19:33 – 19:49 – 20:05	22:02 – 22:19 – 22:28	23:09 – 23:36 – 23:46
$k=3$	20:05 – 20:11 – 22:41	22:28 – 22:37 – 00:55 (+1)	23:46 – 23:57 – 02:04 (+1)

Table 2. Speeds (in m/s) of the crest and the leading and trailing edges of soliton k between two adjacent moorings.

	$v_{\rm L,IW2–IW3}^{(k)} - v_{\rm P,IW2–IW3}^{(k)} - v_{\rm T,IW2–IW3}^{(k)}$	$v_{\rm L,IW1–IW2}^{(k)} - v_{\rm P,IW1–IW2}^{(k)} - v_{\rm T,IW1–IW2}^{(k)}$
$k=1$	1.47 – 1.54 – 1.41	1.39 – 1.53 – 1.57
$k=2$	1.41 – 1.41 – 1.47	1.57 – 1.36 – 1.34
$k=3$	1.47 – 1.45 – 1.57	1.34 – 1.30 – 1.51

5.2. Discussion on reconstruction results

For comparison with the field observations, the temporal variations of the DEPTS-modeled temperatures and sound speeds at all moorings are presented in Fig. 10 with the same format as shown in Fig. 7. Several notable features have been reconstructed in agreement with the experimental results discussed in Subsection 4.2. Specifically, as the packet propagates from IW3 to IW1, shape deformations appear as (i) the increasing amplitudes of solitons 1 and 2 and (ii) the development of additional solitary waves. Packet dispersion is indicated by the apparent temporal spread between the peak arrivals of solitons 1 and 2 as seen from the comparison between Figs. 10(d) and 10(f).

To quantify the accuracy of the proposed DEPTS method, the RMSE between the modeled and observed sound speeds is defined as[15]

$$\mathrm{RMSE}(t;r_{\mathrm{id}})=\sqrt{\frac{1}{M}\sum_{m=1}^{M}\left[\hat{c}(z_m,t;r_{\mathrm{id}})-c(z_m,t;r_{\mathrm{id}})\right]^2}, \quad (45)$$

where M is the number of discrete depth grids, and $\hat{c}(z_m,t;r_{\mathrm{id}})$ and $c(z_m,t;r_{\mathrm{id}})$ are the reconstructed and measured sound speeds, respectively, at depth $z=z_m$ and range $r=r_{\mathrm{id}}$. The RMSEs at IW1, IW2, and IW3 are shown in Figs. 11(a), 11(b), and 11(c), respectively, and the box charts describing the statistics of $\mathrm{RMSE}(t;r_{\mathrm{id}})$ are displayed in Fig. 11(d), where the cross markers denote the mean values of RMSEs.

It can be seen that the reconstruction accuracy at IW1 and IW3 is higher than that at IW2. The means and medians of RMSEs at IW1 and IW3 are below 1.5 m/s, and the maximum RMSEs do not exceed 3 m/s. The third-quartile positions of $\mathrm{RMSE}(t;r_{\mathrm{IW1}})$ and $\mathrm{RMSE}(t;r_{\mathrm{IW3}})$ indicate that 75% of errors remain below 2 m/s. The mean and median RMSEs at IW2 are about 1.7 m/s, and the maximum RMSE is close to 3.5 m/s; the third quartile of $\mathrm{RMSE}(t;r_{\mathrm{IW2}})$ exceeds 2 m/s. Figure 11(b) shows that the larger errors at IW2 are concentrated between 07–10 22:30 and 07–11 00:05. By comparing Figs. 7(b) and 10(b), it is found that the overestimate of temperature by DEPTS during 22:30–00:05(+1) results in the degradation of reconstruction accuracy. There are two possible sources of the modeling errors. First, the mode decomposition may introduce errors into the estimated modal amplitudes of internal waves since the range and time dependency of modal functions $W_1(z)$ are not considered in the present work. Second, the background temperature $\bar{T}(r,z,t)$ in the upper layer ($z<35$ m) is estimated inaccurately from only a few conductivity-temperature-depth (CTD) profiles. The long-term mooring observation is unavailable in the upper ocean due to the limited vertical aperture of an array.

Nevertheless, the proposed method is still effective in reducing the waveform distortion. Three snapshots of the EPTS- and DEPTS-modeled sound-speed fields are shown in Figs. 12(a)–12(c) and 12(d)–12(f), respectively, where the wave peaks of solitons 2 and 3 are annotated by the red arrows. It can be seen from Figs. 12(a) and 12(d) that the shapes of solitons 2 and 3 modeled by the two techniques are both undistorted at 22:13:32. However, the two peaks from EPTS first disappear at 22:54:11 and then appear at 23:28:22 as shown in Figs. 12(b) and 12(c), which is in agreement with the anomalous waveform behavior described in Subsection 2.3.3. By comparison, Figs. 12(d)–12(f) reveal that solitons 2 and 3 in the DEPTS results are always present on the track and propagate without distortion.

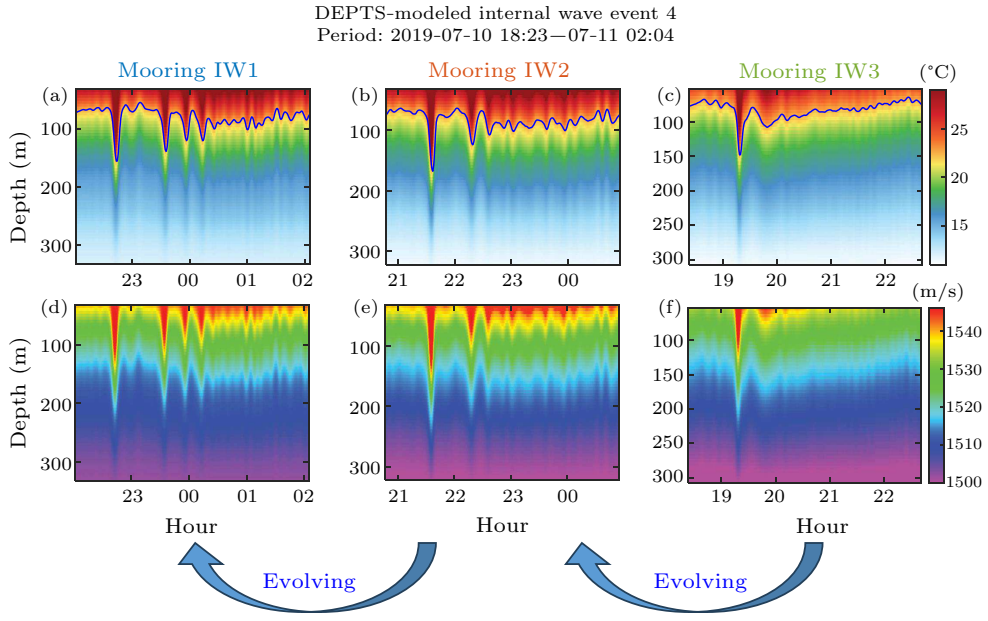


Fig. 10. DEPTS-modeled evolution process of ISW Event 4 from 07–10 18:23 to 07–11 02:04 (UTC+8). The format is the same as Fig. 7.

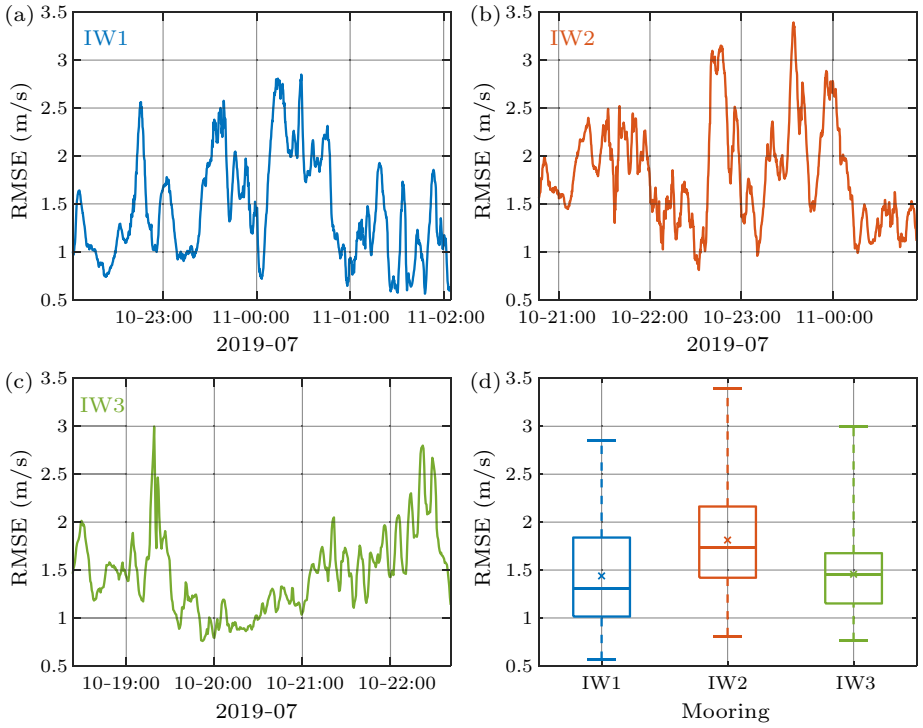


Fig. 11. RMSEs at moorings (a) IW1, (b) IW2, and (c) IW3 and (d) box charts describing the statistics of RMSEs at all moorings. The cross markers in box charts denote the mean values of RMSEs.

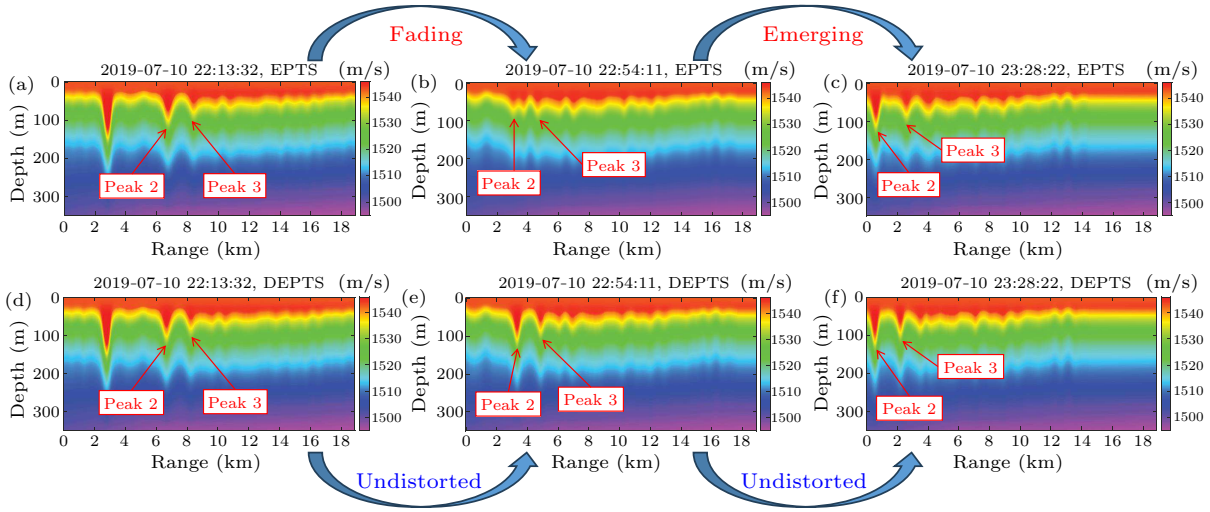


Fig. 12. Sound-speed fields modeled by the EPTS (top row) and DEPTS methods (bottom row) at times [(a), (d)] 2019-07–10 22:13:32, [(b), (e)] 22:54:11, and [(c), (f)] 23:28:22. The wave peaks of solitons 2 and 3 are annotated by the red arrows.

6. Summary and conclusions

This paper proposes the DEPTS model to reconstruct the sound-speed fields perturbed by the deformed and dispersive ISW packets. As a crucial improvement to the existing modeling techniques, packet dispersion is incorporated into DEPTS by assigning the real speed observed in the experiment instead of a common one to each soliton in the wave train.

This study demonstrates that the mismatch between the real and modeled propagation speeds of a soliton causes shape distortions in the reconstructed internal waves and sound speeds. As the wave packet propagates, the distorted waveforms are manifested as the anomalous fade and emergence of the solitary waves whose modeled speeds do not match the real ones. The DEPTS technique takes into account the difference in speeds among individual solitons and mitigates the waveform anomalies.

The practical application of the DEPTS model to the mooring data collected in the SCS shows that the reconstructed sound-speed fields exhibit two important evolving properties of internal waves, i.e., (i) shape deformations including the variations of wave amplitude and the development of solitons in the packet and (ii) packet dispersion manifested as the increasing distance between successive solitons. The above modeled internal-wave features are in good agreement with the field observations, and the waveform distortion inherent

in the original EPTS method is successfully mitigated. At all moorings, the mean and median RMSEs between the DEPTS-modeled and observed sound speeds are below 2 m/s.

Acknowledgments

Project supported by the National Natural Science Foundation of China (Grant Nos. 11534009, 11904342, and 12274348). The authors would like to thank all participants working in the field experiment and the early preparations. Their great efforts contributed to the valuable data for this paper. The authors also thank the GEBCO Compilation Group (2023) GEBCO 2023 Grid (doi:10.5285/f98b053b-0cbc-6c23-e053-6c86abc0af7b) for providing the bathymetry data.

References

[1] Jackson C 2007 *J. Geophys. Res.: Oceans* **112** C11012
[2] Jackson C R, Da Silva J C and Jeans G 2012 *Oceanography* **25** 108
[3] Apel J R, Ostrovsky L A, Stepanyants Y A and Lynch J F 2007 *J. Acoust. Soc. Am.* **121** 695
[4] Lynch J F, Jin G, Pawlowicz R, Ray D, Plueddemann A J, Chiu C S, Miller J H, Bourke R H, Parsons A R and Muench R 1996 *J. Acoust. Soc. Am.* **99** 803
[5] Zhou J X, Zhang X Z and Rogers P H 1991 *J. Acoust. Soc. Am.* **90** 2042
[6] Apel J R 2003 *J. Phys. Oceanogr.* **33** 2247
[7] Finette S, Orr M H, Turgut A, *et al.* 2000 *J. Acoust. Soc. Am.* **108** 957
[8] Duncan A J, Shimizu K, Parnum I M, MacLeod R and Buchan S 2019 *Proceedings of Acoustics*, November 10–13, 2019, Cape Schanck, Victoria, Australia, p. 2
[9] Marshall J, Hill C, Perelman L and Adcroft A 1997 *J. Geophys. Res.: Oceans* **102** 5733
[10] Lermusiaux P F, Xu J, Chen C F, Jan S, Chiu L Y and Yang Y J 2010 *IEEE J. Ocean. Eng.* **35** 895
[11] Duda T F, Lin Y T, Newhall A E, Helfrich K R, Lynch J F, Zhang W G, Lermusiaux P F and Wilkin J 2019 *J. Acoust. Soc. Am.* **146** 1996
[12] Casagrande G, Stephan Y, Varnas A C W and Folegot T 2011 *IEEE J. Ocean. Eng.* **36** 745
[13] Chen P Q, Cheng L, Zhang T, Zhao H F and Li J L 2022 *J. Acoust. Soc. Am.* **152** 2601
[14] Duda T F, Lin Y T and Reeder D B 2011 *J. Acoust. Soc. Am.* **130** 1173
[15] Qu K, 453 Piao S C and Zhu F Q 2019 *Acta Phys. Sin.* **68** 124302 (in Chinese)
[16] Jiang Y Y, Grigorev V and Katsnelson B 2022 *J. Marine Sci. Eng.* **10** 119
[17] Rubenstein D and Brill M H 1991 *Ocean Variability & Acoustic Propagation* (Berlin: Springer) pp 215
[18] Sagers J D 2012 *Predicting acoustic intensity fluctuations induced by nonlinear internal waves in a shallow water waveguide* Ph.D. Dessertation (The University of Texas at Austin Austin)
[19] Sagers J D and Wilson P S 2016 *IEEE J. Ocean. Eng.* **42** 231
[20] Badiey M, Wan L and Song A 2013 *J. Acoust. Soc. Am.* **134** EL7
[21] Frank S D, Badiey M, Lynch J F and Siegmann W L 2004 *J. Acoust. Soc. Am.* **116** 3404
[22] Duda T F and Preisig J C 1999 *IEEE J. Ocean. Eng.* **24** 16
[23] Gerkema T and Zimmerman J T F 2008 *An Introduction to Internal Waves* (Lecture Notes, Royal Netherlands Institute for Sea Research) p. 67
[24] Gill A E 1982 *Atmosphere-Ocean Dynamics* (San Diego: Academic Press) vol 30 p. 159
[25] Yang Y J, Fang Y C, Chang M H, Ramp S R, Kao C C and Tang T Y 2009 *J. Geophys. Res.: Oceans* **114** C10003
[26] Grigorev V A, Katsnelson B G and Lynch J F 2016 *J. Acoust. Soc. Am.* **140** 3980
[27] Weatherall P, Marks K M, Jakobsson M, Schmitt T, Tani S, Arndt J E, Rovere M, Chayes D, Ferrini V and Wigley R 2015 *Earth Space Sci.* **2** 331
[28] Yang J, Zhou S H, Zhou J X and Lynch J F 2004 *IEEE J. Ocean. Eng.* **29** 1054
[29] Fliegel M and Hunkins K 1975 *J. Phys. Oceanogr.* **5** 541
[30] Shaw P T, Ko D S and Chao S Y 2009 *J. Geophys. Res.: Oceans* **114** C02019
[31] Xie J S, He Y H and Cai S Q 2019 *J. Geophys. Res.: Oceans* **124** 4677
[32] Chen L, Xiong X J, Zheng Q A, Yuan Y L, Yu L, Guo Y L, Yang G B, Ju X, Sun J and Hui Z L 2020 *Acta Oceanol. Sin.* **39** 44